Analysis of helical motion coupling effect for the 2-degree-of-freedom Induction Machine

***Abstract*—The 2-degree-of-freedom induction machine realizes rotary, linear and helical motions by itself, which exhibits the merits of integrated structure and high material utilization. Compared with traditional electric machines, one of the special factors affecting the electromagnetic performances is the helical motion coupling effect. This paper investigates the helical motion coupling effect production mechanism based on the proposed helical motion coupling effect mathematical model. The changing rules of coupling effect force in rotary and linear motion parts are then estimated. It can be concluded that the torque performances of the rotary motion component are weakened more than those of the linear motion component by the helical motion coupling effect. Further, two methods to suppress the coupling effect, namely adjustment of linear motion slip ratio and change of the linear motion frequency, are discussed. The experimental results validate the effectiveness of the suppression strategy.**

***Index Terms*—Induction machine, 2-degree-of-freedom, helical motion coupling effect, torque, rotary motion, linear motion.**

I. Introduction

FOR INDUSTRY APPLIATIONS, including pick-and-place robots [1], compressors [2], wave energy harvesters [3] and so on, some special characteristics are needed for the complicated multi-degree-freedom motions of traction system, such as high integration, high reliability and quick response [4-5]. Recently, a new type of 2-degree-of-freedom (2DoF) machine was proposed, which can realize 2D rotary motion, 2D linear motion or 3D helical motion by employing only one motor [6]-[11]. The 2DoF machine is much more integrated and room-saving compared with the traditional rotary-linear motion system due to the absence of intermediate mechanical devices, which can be considered as a promising candidate of traction machines in intelligent industrial systems [12].

However, due to the high integration of multiple motions of the 2DoF machines, there is a helical motion coupling effect existing in the helical motion [13]. It significantly affects the electromagnetic performance, which is one of the key factors hindering the industrial application of these machines. Ebrahim Amiri combines the transient time-domain finite element model and frequency domain slip frequency technique to model the coupling effect caused by dynamic end effects in the rotary armature of the rotary-linear induction motor [14]. Reference [15] uses the design of short magnetic paths to avoid the coupled effect of the linear motion and the rotary movement for a rotary-linear switched-reluctance motor. Besides, a control algorithm based on inductance profiles of the motor phases is proposed to decouple rotary and linear movements of another type of the rotary-linear switched reluctance motor [16]. For the double-stator rotary-linear permanent magnet motor [17], the orthogonal crossed magnetic field caused by the coupling effect is investigated to study the coupling effect degree. Although some results have been achieved, the research of the coupling effect in 2DoF machines is still not systematic and in-depth. Moreover, the analysis of the coupling effect is always based on 3D FEM, which is accurate but time-consuming.

The purpose of this paper is to systematically investigate the influence of helical motion coupling effect on electromagnetic performance of a 2DoF direct drive induction motor (2DoFDDIM), and ultimately to propose suppression strategies for the accurate design. For the 2DoFDDIM the analysis of the characteristics of the rotary, linear and helical motions are presented in [18]. However, the mechanism of the coupling effect should be further investigated. It is worth exploring and comparing the different degrees of the helical motion coupling effect on each motion, which is very useful in the development of the coupling effect suppressing schemes. Thus, the coupling effect production mechanism is investigated, and then the resistant torque and force are calculated based on the helical motion coupling effect mathematical model in sections II and III. In section IV, the influences of the helical motion coupling effect on two motion parts are evaluated and compared. Meanwhile, the key parameters relating to the coupling effect are also analyzed. It is worth noting that the torque performance of the rotary motion part is weakened more seriously. Then, two coupling effect suppression strategies are proposed in Section V, and the 2DoFDDIM prototyped machine is manufactured and tested to verify the effectiveness of the proposed technique. Finally, Section VI draws conclusions.

II. Helical Motion Coupling Effect

The topology of 2DoFDDIM is shown in Fig. 1, which is composed of an integrated stator and a solid mover. It can be found that the stator consists of two arc-shape stator cores, namely the rotary motion and the linear motion stators. The distributed armature windings of rotary and linear parts are wound around the stator teeth, which is similar to the traditional induction machines. For the solid mover, the solid steel is coated with a thin copper layer to enhance the electromagnetic performances of 2DoFDDIM. When the rotary motion stator is powered, the rotating magnetic field is generated, and then the single DoF rotary motion can be achieved. Similarly, the single DoF linear motion can be obtained by an energized linear motion stator. Hence, when two stator parts are powered

simultaneously, both the rotating and the travelling wave magnetic fields will act on the solid mover, and then the 2DoF helical motion is produced.

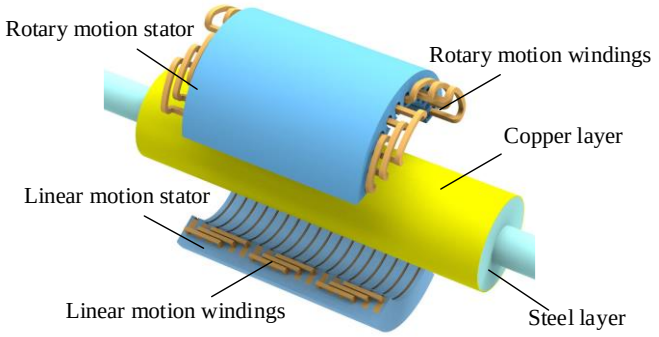

Fig. 1 The topology of 2DoFDDIM.

The topology of linear motion stator is evolved from the rotary motion stator as shown in Fig. 2, where the outer stator diameter D_{so} and inner stator diameter D_{si} of the two parts are identical. The mechanical pole pitch of the linear motion stator τ_{pl} is the same as the rotary motion stator τ_{pr}, which can be calculated as:

$$\tau_{pr} = \tau_{pl} = \frac{l_{a\_r}}{2N_p} = \frac{1}{4N_p}\pi D_{si} \tag{1}$$

where l_{a_r} is the stack length of the rotary motion stator and N_p is the number of pole pairs.

The geometric parameters of 2DoFDDIM are listed in Table I. When the rotary motion and linear motion windings are powered with a 50Hz 220V AC voltage source, the synchronous peripheral speed of rotary motion is 3.9 m/s, which is identical to the synchronous axial velocity of linear motion.

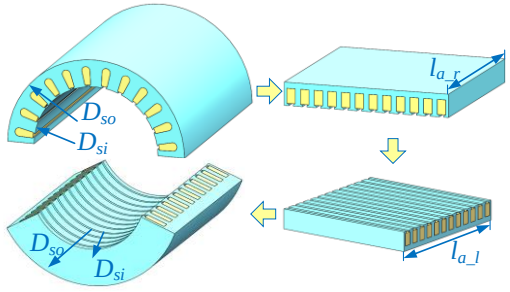

Fig. 2. Evolution of the two motion parts.

TABLE I
GEOMETRIC DIMENSIONS OF THE 2DOFDDIM

Specifications	Rotary part	Linear part
Stator slots number N_s	12	
Pole pairs number N_p	2	
Stator outer diameter D_{so} (mm)	155	
Stator inner diameter D_{si} (mm)	100	
Rotor outer diameter D_{ro} (mm)	94	
Air gap length g (mm)	2.5	
Stack length l_{a_r} l_{a_l} (mm)	157	135
Pole pitch τ_p (mm)	39.25	
Copper layer thickness l_{cu} (mm)	1.2	
Iron lamination type	A3 steel	
Number of turns per coil	90	

Table II lists the average no-load rotating speed and locked torque of the 2DoFDDIM with single DoF rotary motion (only the rotary motion stator is powered) and 2DoF helical motion with the axial velocity of 3.9 m/s, 3.12 m/s, 2.34 m/s, 1.56 m/s, 0.78 m/s or 0 m/s (the power is supplied for both motion stators). For the single DoF rotary motion, the no-load rotating speed is 792 r/min, which is higher than the ideal synchronous speed 750 r/min, since the effective electromagnetic pole pitch τ_{ep} is longer than that of the mechanical size τ_p, as shown in Fig. 3. The air-gap flux density distributions of rotary motion components at rated $s_r = 0.2$ are derived using FEM. It can be seen that the flux density decays rapidly to zero within a certain range outside the two ends of the stator due to the end effect [19].

However, the no-load rotating speed of the 2DoFDDIM with helical motion is smaller than that with corresponding single DoF rotary motion as listed in Table II. Moreover, the average locked torque of the motor with the single DoF rotary motion is higher than that with helical motion. For example, the average locked torque of the motor with single DoF rotary motion is 12 Nm, which is 1.1 times that with helical motion when axial velocity is 3.12 m/s. Besides, the no-load rotating speed and average locked torque of the motor with helical motion increases with the decrease of the axial velocity. Hence, it concludes that the resistant torque is produced due to the linear motion component, which contributes to deteriorating the rotary motion performances and increases with the increase of the axial velocity.

TABLE II
AVERAGE NO-LOAD ROTATING SPEED AND LOCKED TORQUE OF THE 2DOFDDIM

	Average no-load rotating speed	Average locked torque
R	792.38 r/min	12 Nm
H_R_L3.9	651.18 r/min	10.94 Nm
H_R_L3.12	660.99 r/min	11 Nm
H_R_L2.34	669.51 r/min	11.12 Nm
H_R_L1.56	678.99 r/min	11.36 Nm
H_R_L0.78	682.58 r/min	11.41 Nm
H_R_L0	689.56 r/min	11.43 Nm

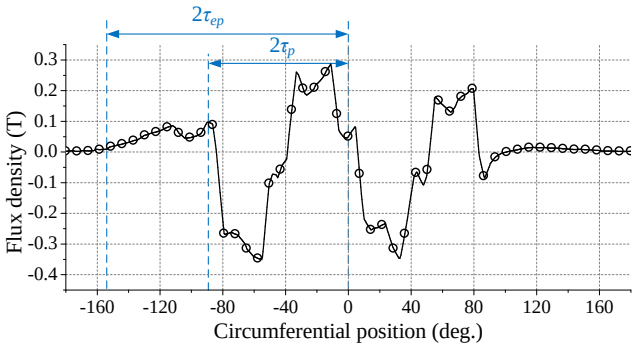

Fig.3. Air gap flux density of the rotary motion part.

The average no-load linear velocity and locked force of the 2DoFDDIM with single DoF linear motion (only the linear motion stator is powered) and 2DoF helical motion with rotating speed of 750 r/min, 600 r/min, 450 r/min, 300 r/min, 150 r/min or 0 r/min (the power is supplied for both motion stators) are listed in Table III. Same as the analysis for the rotary motion, the no-load linear velocity (4.03 m/s) is higher than the ideal synchronous velocity 3.92 m/s on account of the effective electromagnetic pole pitch shown in Fig.4. Moreover, the resistant force is generated due to the rotary motion

component, which deteriorates the linear motion performances and increases with the increase of the rotary speed. For example, the average no-load axial velocity of single DoF linear motion is 4.03 m/s, which is 1.06 times that of the helical motion with n_r=600 r/min (3.81 m/s).

TABLE III
NO-LOAD AXIAL VELOCITY OF THE 2DOFDDIM

	No-load velocity of linear motion	
L	4.03 m/s	307.67 N
H_L_R750	3.80 m/s	302.08 N
H_L_R600	3.81 m/s	304.66 N
H_L_R450	3.84 m/s	300.95 N
H_L_R300	3.88 m/s	303.79 N
H_L_R150	3.90 m/s	307.27 N
H_L_R0	3.92 m/s	307.31 N

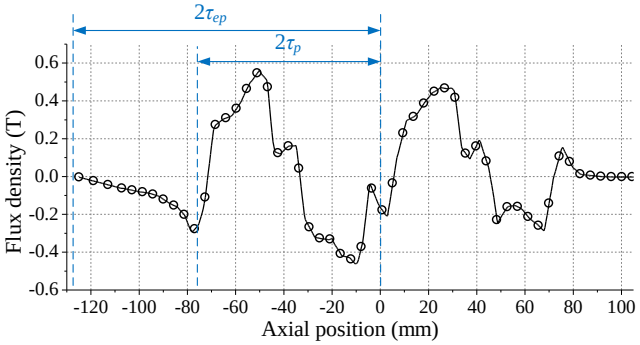

Fig.4. Air gap flux density of the linear motion part.

Therefore, the resistant torque and force are identified as the key parameters to evaluate the influence of the coupling effect on electromagnetic performances of 2DoF helical motion in 2DoFDDIM.

III. HELICAL MOTION COUPLING EFFECT MATHEMATICAL MODEL

To calculate the resistant torque and force, the helical motion coupling effect mathematical model is derived based on the expanded model as shown in Fig. 5. The following assumptions are made:

(1) The end effect of both stator parts are ignored.
(2) The curvature of the mover is ignored.
(3) Only the fundamental components of armature reaction flux density are considered.

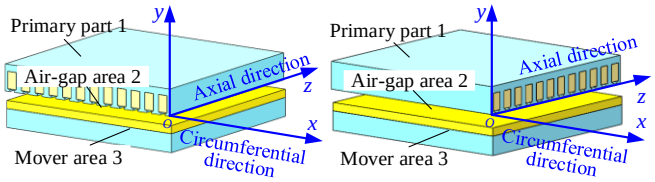

(a) (b)

Fig. 5. The expanded model of the 2DoFDDIM. (a) The rotary motion part. (b) The linear motion part.

When the mover produces rotary motion, the speed $\vec{V}$ only consists of the circumferential component V_x (peripheral speed). Besides, the armature reaction flux density B_x, and the induced voltage E_x is produced in the mover. When the mover produces linear motion, only the axial components V_z, B_z and E_z exist in the mover. For the helical motion, $\vec{V}=V_x\vec{i}+V_z\vec{k}$. Moreover, B_y and E_y will be induced except circumferential and axial components. Therefore, it can be derived that $\vec{B}=B_x\vec{i}+B_y\vec{j}+B_z\vec{k}$ and $\vec{E}=E_x\vec{i}+E_y\vec{j}+E_z\vec{k}$.

The electromagnetic force density $\vec{F}$ can be calculated as shown in (2):

$$\vec{F}=\vec{J}\times\vec{B} \tag{2}$$

where, $\vec{J}$ is the current density, $\vec{J}=\sigma(\vec{E}+\vec{V}\times\vec{B})$. σ is the conductivity. Thus, it can be derived from (2) that

$$\begin{aligned}\vec{F}&=\sigma(\vec{E}+\vec{V}\times\vec{B})\times\vec{B}=\sigma(-\frac{\partial\vec{A}}{\partial t}\times\vec{B}+\vec{V}\times\vec{B}\times\vec{B})\\&=\sigma(\begin{vmatrix}\vec{i}&\vec{j}&\vec{k}\\B_x&B_y&B_z\\\frac{\partial A_x}{\partial t}&\frac{\partial A_y}{\partial t}&\frac{\partial A_z}{\partial t}\end{vmatrix}+\begin{vmatrix}\vec{i}&\vec{j}&\vec{k}\\-V_zB_y&-V_xB_z+V_zB_x&V_xB_y\\B_x&B_y&B_z\end{vmatrix})\\&=\sigma(-V_xB_z^2+V_zB_xB_z-V_xB_y^2+B_y\frac{\partial A_z}{\partial t}-B_z\frac{\partial A_y}{\partial t})\vec{i}\\&+\sigma(B_z\frac{\partial A_x}{\partial t}-B_x\frac{\partial A_z}{\partial t}+V_xB_xB_y+V_zB_yB_z)\vec{j}\\&+\sigma(-V_zB_y^2+V_xB_xB_z-V_zB_x^2+B_x\frac{\partial A_y}{\partial t}-B_y\frac{\partial A_x}{\partial t})\vec{k}\end{aligned} \tag{3}$$

For the rotary motion, V_z=B_z=A_x=A_y=0, thus the electromagnetic force in the circumferential direction is

$$\overrightarrow{F_x}=\sigma(-V_xB_y^2+B_y\frac{\partial A_z}{\partial t})\vec{i}+\sigma(-B_x\frac{\partial A_z}{\partial t}+V_xB_xB_y)\vec{j} \tag{4}$$

For the linear motion, V_x=B_x=A_z=A_y=0. Then the electromagnetic force of axial direction is

$$\overrightarrow{F_z}=\sigma(B_z\frac{\partial A_x}{\partial t}+V_zB_yB_z)\vec{j}+\sigma(-V_zB_y^2-B_y\frac{\partial A_x}{\partial t})\vec{k} \tag{5}$$

Hence, the interacting electromagnetic force (torque) of the helical motion can be expressed as:

$$\begin{aligned}\Delta\overrightarrow{F}&=\vec{F}-\overrightarrow{F_x}-\overrightarrow{F_z}=\Delta F_x\vec{i}+\Delta F_z\vec{k}\\&=\sigma(-V_xB_z^2+V_zB_xB_z-B_z\frac{\partial A_y}{\partial t})\vec{i}\\&+\sigma(V_xB_xB_z-V_zB_x^2+B_x\frac{\partial A_y}{\partial t})\vec{k}\end{aligned} \tag{6}$$

where $\vec{A}$ is the vector magnetic potential, $\vec{A}=A_x\vec{i}+A_y\vec{j}+A_z\vec{k}$, and $\vec{E}=-\frac{\partial\vec{A}}{\partial t}$, $\vec{B}=\nabla\times\vec{A}$. Moreover,

$$\begin{aligned}\nabla^2\vec{A}&=-\mu\vec{J}=-\mu\sigma(\vec{E}+\vec{V}\times\vec{B})\\&=\mu\sigma(\frac{\partial\vec{A}}{\partial t}-\vec{V}\times(\nabla\times\vec{A}))\end{aligned} \tag{7}$$

where μ represents the permeability. Thus, the x, y and z components of $\nabla^2\vec{A}$ can be obtained, respectively.

$$\begin{cases} \nabla^2 A_x = \mu\sigma\left[\dfrac{\partial A_x}{\partial t} + V_z(\dfrac{\partial A_x}{\partial z} - \dfrac{\partial A_z}{\partial x})\right] \\ \nabla^2 A_y = \mu\sigma\left[\dfrac{\partial A_y}{\partial t} - V_z(\dfrac{\partial A_z}{\partial y} - \dfrac{\partial A_y}{\partial z}) + V_x(\dfrac{\partial A_y}{\partial x} - \dfrac{\partial A_x}{\partial y})\right] \\ \nabla^2 A_z = \mu\sigma\left[\dfrac{\partial A_z}{\partial t} - V_x(\dfrac{\partial A_x}{\partial z} - \dfrac{\partial A_z}{\partial x})\right] \end{cases} \quad (8)$$

To obtain the helical motion coupling effect mathematical model, the calculation process of ΔF for 2DoFDDIM is derived based on the following two parts.

(a). It is assumed that the helical motion is produced by the stator current in the direction of z axis (excited rotary motion stator) and the external axial movement is presented on the mover (no power for linear motion stator). Therefore, in the mover area, $\dfrac{\partial \overrightarrow{A_r}}{\partial z} = 0$. The electromagnetic field equation, in terms of $\overrightarrow{A_r}$ can be expressed as

$$\begin{cases} \nabla^2 A_{xr} = \mu\sigma\left(\dfrac{\partial A_{xr}}{\partial t} - V_z\dfrac{\partial A_{zr}}{\partial x}\right) \\ \nabla^2 A_{yr} = \mu\sigma\left[\dfrac{\partial A_{yr}}{\partial t} - V_z\dfrac{\partial A_{zr}}{\partial y} + V_x(\dfrac{\partial A_{yr}}{\partial x} - \dfrac{\partial A_{xr}}{\partial y})\right] \\ \nabla^2 A_{zr} = \mu\sigma\left(\dfrac{\partial A_{zr}}{\partial t} + V_x\dfrac{\partial A_{zr}}{\partial x}\right) \end{cases} \quad (9)$$

where the parameters with subscript r refer to the situation where only rotary motion stator is excited. Considering the boundary conditions,

$$\begin{cases} H_{2xr} = -J_r = -J_{mr}e^{j(\omega_r t - \beta_r x)} \\ A_{2xr} = A_{2yr} = 0 \qquad\qquad , y = 0 \\ B_r = B_{mr}e^{j(\omega_r t - \beta_r x)} \end{cases} \quad (10)$$

$$\begin{cases} B_{2yr} = B_{3yr} \\ H_{2xr} = H_{3xr} \end{cases}, y = g \ \&\ A_{3xr} = A_{3yr} = A_{3zr} = 0, y \to \infty$$

where the parameters with subscript 2 and 3 refer to the air gap area and mover area in Fig.5, respectively. g is the thickness of the air gap, J_{mr} and B_{mr} are the amplitudes of current density and armature reaction flux density. ω_r is the synchronous angular speed, $\omega_r = \beta_r V_{1x}$, V_{1x} is the synchronous rotating peripheral speed. $\beta_r = \pi/\tau_{epr}$, τ_{epr} is the electromagnetic pole pitch of the rotary motion part. Then the vector magnetic potential $\overrightarrow{A_{2r}}$ in air gap area and $\overrightarrow{A_{3r}}$ in mover area can be derived.

$$\overrightarrow{A_{2r}} = A_{2xr}\vec{i} + A_{2yr}\vec{j} + A_{2zr}\vec{k} \quad (11)$$

$$\begin{cases} A_{2xr} = 0 \\ A_{2yr} = 0 \\ A_{2zr} = \dfrac{\mu_0 J_{mr}}{\beta_r \gamma'_r}[ch\beta_r(y-g) - \dfrac{\alpha_{zr}\mu_0}{\mu_3\beta_r}sh\beta_r(y-g)]e^{j(\omega_r t - \beta_r x)} \end{cases} \quad (12)$$

$$\overrightarrow{A_{3r}} = A_{3xr}\vec{i} + A_{3yr}\vec{j} + A_{3zr}\vec{k} \quad (13)$$

$$\begin{cases} A_{3xr} = -\dfrac{V_z}{V_x}\dfrac{\mu_0 J_{mr}}{\beta_r \gamma'_r}[e^{-\alpha_{zr}(y-g)} - se^{-\alpha_{xr}(y-g)}]e^{j(\omega_r t - \beta_r x)} \\ A_{3yr} = j\dfrac{V_z}{V_x}\dfrac{\mu_0 J_{mr}}{\beta_r \gamma'_r}\dfrac{\beta_r}{\alpha_{zr}}[e^{-\alpha_{zr}(y-g)} - s\dfrac{\alpha_{zr}}{\alpha_{xr}}e^{-\alpha_{xr}(y-g)}]e^{j(\omega_r t - \beta_r x)} \\ A_{3zr} = \dfrac{\mu_0 J_{mr}}{\beta_r \gamma'_r}e^{-\alpha_{zr}(y-g)}e^{j(\omega_r t - \beta_r x)} \end{cases} \quad (14)$$

where $V_x = (1-s_r)V_{1x}$, V_z is the axial velocity, μ_0 is the air permeability, $\gamma'_r = sh(\beta_r g) + \alpha_{zr}\mu_0 ch(\beta_r g)/(\beta_r \mu_3)$, $\alpha^2_{zr} = \beta^2_r + js_r\omega_r\mu_3\sigma_3$, and $\alpha^2_{xr} = \beta^2_r + j\omega_r\mu_3\sigma_3$. μ_3 and σ_3 refer to the permeability and conductivity of the mover. It can be noted that the decaying terms with α_{xr} decay faster than those with α_{zr}. To simplify the analysis, only the components with α_{zr} are considered in the following sections. Then according to $\vec{B} = \nabla \times \vec{A}$, the magnetic flux density $\overrightarrow{B_{3r}}$ in the mover area can be derived.

$$\overrightarrow{B_{3r}} = B_{3xr}\vec{i} + B_{3yr}\vec{j} + B_{3zr}\vec{k} \quad (15)$$

$$\begin{cases} B_{3xr} = -\alpha_{zr}\dfrac{\mu_0 J_{mr}}{\beta_r \gamma'_r}e^{-\alpha_{zr}(y-g)}e^{j(\omega_r t - \beta_r x)} \\ B_{3yr} = j\dfrac{\mu_0 J_{mr}}{\gamma'_r}e^{-\alpha_{zr}(y-g)}e^{j(\omega_r t - \beta_r x)} \\ B_{3zr} = -\dfrac{j\mu_3\sigma_3 s\omega_r}{\alpha_{zr}}\dfrac{\mu_0 J_{mr}}{\beta_r \gamma'_r}\dfrac{V_z}{V_x}e^{-\alpha_{zr}(y-g)}e^{j(\omega_r t - \beta_r x)} \end{cases} \quad (16)$$

By substituting $\overrightarrow{A_{3r}}$ and $\overrightarrow{B_{3r}}$ into (6), the resistant torque or force under powered rotary motion part and mechanical axial motion can be derived.

$$\begin{cases} \Delta F_{x\_Lnopower} = -j\mu_3\beta_r(\sigma_3 V_z\dfrac{s_r}{1-s_r}\dfrac{\mu_0 J_{mr}}{\alpha_{zr}\gamma'_r}e^{-\alpha_{zr}(y-g)}e^{j(\omega_r t - \beta_r x)})^2 \\ \qquad\qquad = j\mu_3\beta_r(\sigma_3 V_z\dfrac{s_r}{1-s_r}\dfrac{B_{mr}}{\alpha_{zr}\gamma_r}e^{-\alpha_{zr}(y-g)}e^{j(\omega_r t - \beta_r x)})^2 \\ \Delta F_{z\_Lnopower} = V_z\sigma_3\dfrac{s_r}{1-s_r}(\dfrac{\mu_0 J_{mr}}{\gamma'_r}e^{-\alpha_{zr}(y-g)}e^{j(\omega_r t - \beta_r x)})^2 \\ \qquad\qquad = -V_z\sigma_3\dfrac{s_r}{1-s_r}(\dfrac{B_{mr}}{\gamma_r}e^{-\alpha_{zr}(y-g)}e^{j(\omega_r t - \beta_r x)})^2 \end{cases} \quad (17)$$

where $\gamma_r = ch(\beta_r g) + \alpha_{zr}\mu_0 sh(\beta_r g)/(\beta_r \mu_3)$. $\Delta F_{x\_Lnopower}$ is defined as the resistant torque produced by the axial movement and $\Delta F_{z\_Lnopower}$ is the resistant force caused by the rotating magnetic field.

(b). It is assumed that the stator current only consists of the circumferential component (equivalent to x axis, namely only linear motion stator is powered) and the externally rotating movement is acting on the mover. The analyzing process is similar to part (a). The electromagnetic field equation in terms of $\overrightarrow{A_l}$ can be expressed as

$$\begin{cases} \nabla^2 A_{xl} = \mu\sigma\left(\dfrac{\partial A_{xl}}{\partial t} - V_z \dfrac{\partial A_{zl}}{\partial x}\right) \\ \nabla^2 A_{yl} = \mu\sigma\left[\dfrac{\partial A_{yl}}{\partial t} - V_z \dfrac{\partial A_{zl}}{\partial y} + V_x\left(\dfrac{\partial A_{yl}}{\partial x} - \dfrac{\partial A_{xl}}{\partial y}\right)\right] \\ \nabla^2 A_{zl} = \mu\sigma\left(\dfrac{\partial A_{zl}}{\partial t} + V_x \dfrac{\partial A_{zl}}{\partial x}\right) \end{cases} \quad (18)$$

Under this situation, the interacting resistant force (torque) produced by rotating movement and travelling wave magnetic field can be expressed as

$$\begin{cases} \Delta F_{x\_Rnopower} = V_x^2 \cdot j\mu_3\beta_l(\sigma_3 s_l \dfrac{V_{1z}}{V_z}\dfrac{B_{ml}}{\alpha_{zl}\gamma_l} e^{-\alpha_{zl}(y-g)} e^{j(\omega_l t-\beta_l z)})^2 \\ \Delta F_{z\_Rnopower} = -V_x \cdot \sigma_3 s_l \dfrac{V_{1z}}{V_z}(\dfrac{B_{ml}}{\gamma_l} e^{-\alpha_{zl}(y-g)} e^{j(\omega_l t-\beta_l z)})^2 \end{cases} \quad (19)$$

where, the parameters with subscript *l* refer to the situation that only linear motion stator is excited. $\Delta F_{x\_Rnopower}$ is defined as the resistant torque produced by travelling wave magnetic field and $\Delta F_{z\_Rnopower}$ is the resistant force caused by rotating movement.

To sum up the two parts, the resistant torque ΔF_x in rotary motion part and the resistant force ΔF_z in linear motion part can be derived as (20).

$$\begin{cases} \Delta F_x = \Delta F_{x\_Lnopower} + \Delta F_{x\_Rnopower} \\ \Delta F_z = \Delta F_{z\_Lnopower} + \Delta F_{z\_Rnopower} \end{cases} \quad (20)$$

Thus, equations (17), (19) and (20) together constitute the helical motion coupling effect mathematical model. By applying this model, the resistant torques with rotating speed n_r=600 r/min (the rated slip ratio s_r=0.2) at different linear velocities are calculated, as shown in Fig. 6. It can be found that the analytical $\Delta F_{x\_Rnopower}$ increases with the rise of axial velocity, which verifies the conclusions draw from (17) to (20). The trends of analytical $\Delta F_{x\_Rnopower}$ and $\Delta F_{x\_Lnopower}$ are consistent with those of the FEA results, while the analytical values are higher than the FEA results as shown in Fig. 6(a). The reason is the simplified equivalent analysis of the motor expanded model, in which the displacement current and magnetic saturation are neglected.

As shown in Fig. 6(b), both the sum of the resistant torque $\Delta F_{x\_Rnopower}$ and $\Delta F_{x\_Lnopower}$ calculated by the helical motion mathematical model and FEA show the same tendency compared with the trend of ΔF_x derived by FEA directly. Moreover, it can be found that the $\Delta F_{x\_Rnopower}$+$\Delta F_{x\_Lnopower}$ by FEA is slightly lower than the resistant torque ΔF_x in helical motion, which is because the magnetic fields of two motion parts are coupled at the end regions of the stator. In this case, the value of $\Delta F_{x\_Rnopower}$+$\Delta F_{x\_Lnopower}$ calculated by (20) at rated s_r=s_l=0.2 is 2.3 Nm, which is 1.2 times that of ΔF_x by FEA.

Similarly, for the helical motion with the axial velocity v_l=3.12 m/s (s_l=0.2), the resistant forces with different rotating speeds are shown in Fig. 7. The resistant force increases as the rotating speed rises. The trends of $\Delta F_{z\_Rnopower}$, $\Delta F_{z\_Lnopower}$ and $\Delta F_{z\_Rnopower}$+$\Delta F_{z\_Lnopower}$ obtained by the helical motion coupling effect mathematical model are agreed well with the corresponding FEA results. For the rated condition with s_r=s_l=0.2, the resistant force ΔF_z is 20N, which is approximately identical to the sum of $\Delta F_{x\_Rnopower}$ and $\Delta F_{x\_Lnopower}$ calculated by FEA.

Therefore, the resistant torque and force (ΔF_x and ΔF_x), which are considered as important indexes for evaluating the coupling effect in helical motion of the 2DoFDDIM, and their trends can be effectively predicted by the helical motion coupling effect mathematical model.

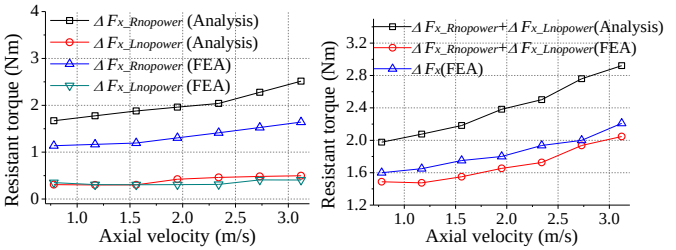

Fig. 6. The resistant torque with different axial velocities. (a) $\Delta F_{x\_Rnopower}$ and $\Delta F_{x\_Lnopower}$. (b) Total resistant torque ΔF_x.

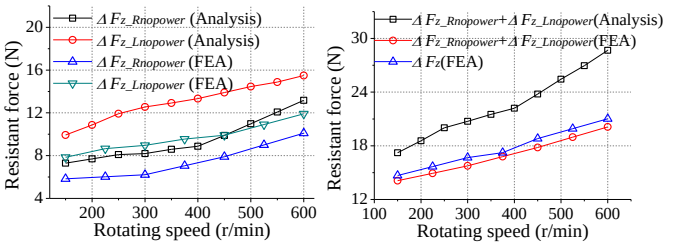

Fig. 7. The resistant force with different rotating speeds. (a) $\Delta F_{z\_Rnopower}$ and $\Delta F_{z\_Lnopower}$. (b) Total resistant force ΔF_z.

IV. Electromagnetic Performances Comparison

To further evaluate the influence of the helical motion coupling effect, a comprehensive comparison of the performance between the rotary and linear motion parts is conducted.

Two motion parts of 2DoFDDIM are designed with the same D_{so}, D_{si}, τ_p and power source, as listed in Table I. Then the synchronous peripheral speed of rotary motion is set equal to the synchronous axial velocity as above. Hence, V_x is equal to V_z at the same slip ratio in the helical motion coupling effect mathematical model.

The influence of resistant torque (force) can be evaluated by the key parameters of the resistant torque ratio k_{RT} and the resistant torque ratio k_{RF}, which are expressed as:

$$k_{RT} = \frac{\Delta F_x}{F_x} \quad (21)$$

$$k_{RF} = \frac{\Delta F_z}{F_z} \quad (22)$$

The resistant torque ratio k_{RT} at different linear motion slip ratios s_l and rotary motion slip ratios s_r are shown in Fig. 8. It can be found that k_{RT} with the same s_r decreases as the s_l increases. For the rated s_r=0.2, k_{RT} is 77% at s_l=0, which is 38% higher than the case with s_l=1. Hence, k_{RT} is significantly affected by the axial velocity of linear motion.

For the linear motion component of helical motion, k_{RF}

decreases with the increase of s_r at the same s_l as shown in Fig. 9. For instance, when s_l=0.2, k_{RF} is 27% at s_r=0, which is 2.5 times that of s_r=1. Besides, with the same s_r, the larger the s_l is, the lower the k_{RF} will be, which is similar to the trend of k_{RT} in the rotary motion component.

Furthermore, k_{RT} is significantly higher than k_{RF} when the slip ratios of two motions are identical, i.e. s_r=s_l as shown in Fig. 10. The overall performance comparison of the two motion components is presented in Table IV. For example, at the rated slip ratio s_r=s_l=0.2, k_{RT} is 64%, which is 3.6 times of k_{RF}. Hence, the torque performance of the rotary motion component is worsened more seriously than that of linear motion component by the helical motion coupling effect, for which the reason can be explained based on the helical motion coupling effect mathematical model. As has been stated in Section Ⅲ, the resistant torque and force ΔF_x and ΔF_z are composed of $\Delta F_{x\_Rnopower}$, $\Delta F_{x\_Lnopower}$ and $\Delta F_{z\_Rnopower}$, $\Delta F_{z\_Lnopower}$, respectively. They are dominantly determined by the parameters of the two motion parts, including velocity V, frequency f, slip ratio s, armature reaction flux density B_m, and effective electromagnetic pole pitch τ_{ep}. Meanwhile, the B_m of the two motion parts is also influenced by the slip ratio.

With the same power sources, operating slip ratios(s_r=s_l) and approximately equal values of the effective electromagnetic pole pitch for the two motion parts, the flux density B_m is considered as the dominant component influencing ΔF_x and ΔF_z. As shown in Fig. 11, the flux density fundamental harmonic amplitude B_{mr} is 0.32 T for the single DoF rotary motion with slip ratio s_r=0.2, which is 1.18 times that for the rotary motion component of 2DoF helical motion with s_r=s_l=0.2. For the linear motion component of helical motion, B_{ml} is 0.38 T at s_r=s_l=0.2, which is approximately identical to that of the single DoF linear motion with s_l=0.2. Based on the helical motion coupling effect mathematical model, B_{mr} and B_{ml} are proportional to ΔF_x and ΔF_z, respectively. Therefore, it can be concluded that B_{mr} is weakened significantly by the linear motion, while B_{ml} is slightly influenced by the rotary motion, which is the key reason of the higher deterioration of rotating torque performance than linear force performance. Besides, the B_{mr} of helical motion at s_r=s_l=0.2 is only 71% of B_{ml}. Hence, ΔF_x is larger than ΔF_z according to (17) and (19). Further, the F_z of linear motion is 111 N, which is 1.3 times of F_x. Therefore, compared with the linear motion component, the k_{RT} of rotary motion component is higher than the k_{RF}.

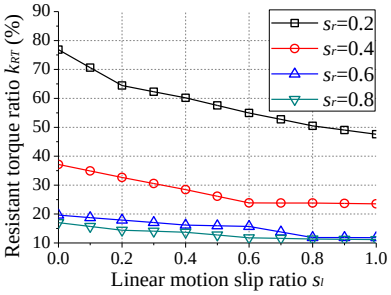

Fig. 8. The resistant torque ratio at different s_r and s_l.

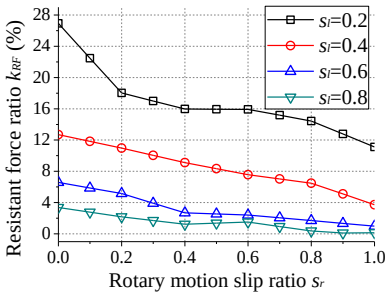

Fig. 9. The resistant force ratio at different s_r and s_l.

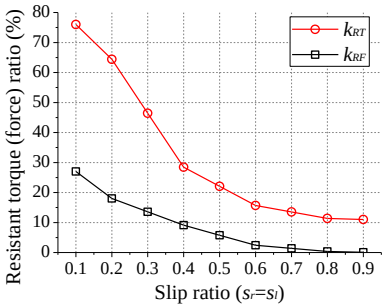

Fig. 10. The resistant force and torque ratios at the same slip ratios.

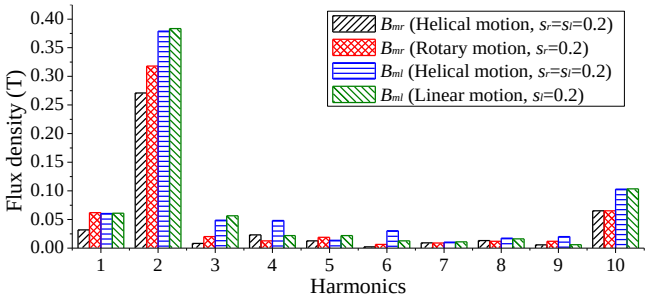

Fig. 11. The harmonic distributions of the air gap flux density of two motion parts.

TABLE IV
PERFORMANCES COMPARISON OF TWO MOTION PARTS

Items	Rotary part	Linear part
Frequency, f (Hz)	50	50
Synchronous rotary speed (r/min)	750	—
Synchronous axial (peripheral) velocity (m/s)	3.9	3.9
No load rotating speed at s_l=0.2 (r/min)	662	—
No load axial velocity at s_r=0.2 (m/s)	—	3.81
Axial (linear) velocity at s_r=s_l=0.2 (m/s)	3.12	3.12
Electromagnetic pole pitch, τ_{epr}, τ_{epl} (mm)	130.3	128
Armature reaction flux density, B_{mr}, B_{ml} (T)	0.27	0.38
Resistant torque (force) ratio, k_{RT}, k_{RF} (%)	64	18

With different s_r and s_l, the B_{mr} and B_{ml} of the helical motion are shown in Fig. 12. It can be found that B_{mr} increases as s_l rises, since the helical motion coupling effect is weakened in rotary motion part when the linear velocity is low. For the linear motion part, B_{ml} are approximately identical at different s_r. In this case, ΔF_x and ΔF_z should take the rotating speed and axial velocity into consideration in (17) and (19). For the helical motion with rated rotary slip ratio s_r=0.2, the k_{RT} at different s_l is changed from 47% to 77%. Nevertheless, the range of k_{RF} at s_l=0.2 is from 12% to 27%, which is significantly lower than that of the k_{RT}. Therefore, it is verified that the electromagnetic performance of the rotary motion component is weakened more

seriously than that of the linear motion component due to the helical motion coupling effect, which should take a key consideration in the coupling effect suppression of the 2DoFDDIM.

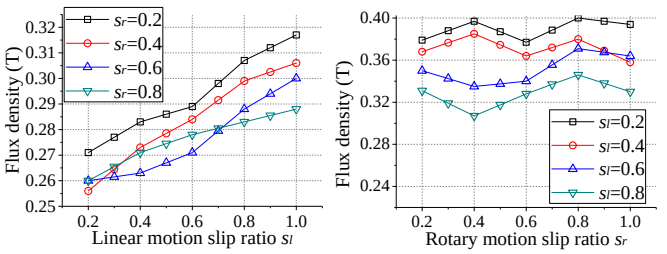

(a) (b)

Fig. 12. The flux density of two parts at different s_r and s_l. (a) The rotary motion part. (b) The linear motion part.

V. Coupling Effect Suppression

Based on the helical motion coupling effect mathematical model in Section III, $\Delta F_{x\_Rnopower}$ is considered as the dominant component of resistant torque ΔF_x because it holds a large percentage of ΔF_x than that of $\Delta F_{x\_Lnopower}$. For example, the $\Delta F_{x\_Rnopower}$ of the helical motion with rated s_r=s_l=0.2 is 37 N, which is significantly higher than the corresponding $\Delta F_{x\_Lnopower}$ (4.3N). From (17), $\Delta F_{x\_Rnopower}$ is directly proportional to the axial velocity V_z and the armature reaction flux density B_{ml}. Meanwhile, B_{ml} decreases with the increase of the linear motion slip ratio s_l, which contributes to reducing the main $\Delta F_{x\_Rnopower}$ further. Hence, by reducing the key parameter V_z, the coupling effect in rotary motion part can be suppressed. Two methods are discussed in this section, including adjustment of the linear motion slip ratio and change of the linear motion frequency. Both are verified by FEA.

A. Adjustment of linear motion slip ratio

The higher linear slip ratio s_l=0.8 is chosen as an example, then the electromagnetic performances of 2DoFDDIM with s_l=0.2 and s_l=0.8 are compared in Table V. It can be found that the no-load rotating speed is 682 r/min at s_l=0.8, which is 3% higher than that of s_l=0.2. Besides, the output torque of helical motion at s_r=0.2 and s_l=0.8 is 1.77 Nm, which is 1.38 times that when s_r=s_l=0.2, thus, k_{RT} is decreased by 18%. Meanwhile, k_{RF}=3% is declined dramatically at s_r=0.2 and s_l=0.8 due to the reduction of axial velocity. Therefore, it can be concluded from Table V that improvement of the s_l can reduce the resistant torque ratio to some extent but the reduced k_{RT} is not small enough. Moreover, the resistant force ratio is also decreased but the deterioration of the electromagnetic performance for the linear motion component of the 2DoFDDIM usually associates with the high s_l which should be considered when using this method.

TABLE V
PERFORMANCES OF 2DOFDDIM AT DIFFERENT LINEAR MOTION SLIP RATIOS

Items	Linear motion slip ratios	
	s_l=0.2	s_l=0.8
Frequency, f (Hz)	50	50
No-load rotating speed, $v_{\_noload}$ (r/min)	662	682
Output torque at s_r=0.2, T_{out} (Nm)	1.28	1.77
Resistant torque at s_r=0.2 (Nm)	2.3	1.81
Resistant torque ratio at s_r=0.2, k_{RT} (%)	64	50
Output force at s_r=0.2 (N)	91	267
Resistant force at s_r=0.2 (N)	20	8.2
Resistant force ratio at s_r=0.2, k_{RF} (%)	18	3

B. Change of the linear motion frequency

The axial velocity can be reduced by adjusting the frequency of linear motion to improve the coupling effect suppression ability. Fig. 13 show k_{RT} and k_{RF} at different linear motion frequencies f_l, where the rotary motion frequency f_r is a constant value of 50 Hz, and the slip ratio of two motion parts are identical to 0.2. It can be seen that the trends of analysis results by helical motion coupling effect mathematical model is similar to the FEA results. Besides, it is worth noting that k_{RT} declines while the k_{RF} increases as the linear motion frequency decreases, and k_{RT}=k_{RF} is obtained at around 25 Hz. Hence, the linear motion frequency f_l=25Hz is chosen, k_{RT} and k_{RF} are 23% and 25%, respectively.

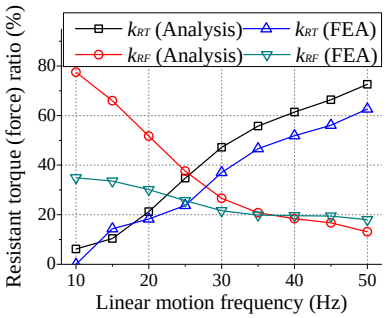

Fig. 13. The resistant torque and force ratio versus different linear motion frequencies (s_r=s_l=0.2, f_r=50Hz).

The output torque per-unit values and k_{RT} at different s_r are shown in Fig. 14, where the base torque value is chosen as the locked torque of rotary motion (11 Nm). It can be found that the output torque with f_l=25 Hz is 2.6 Nm at rated s_r=s_l=0.2, which is 2.03 times that when f_l=50Hz. Meanwhile, the 64% reduction of k_{RT} is obtained. Hence, the helical motion coupling effect is suppressed effectively in rotary motion part.

However, k_{RF}=25% with f_l=25Hz is 1.38 times that with f_l=50Hz at rated s_r=s_l=0.2 as shown in Fig.15. The reason is the influence produced by the rotary motion on the traveling wave magnetic field enhances as the linear motion frequency decreases, then the helical motion coupling effect is strengthened in the linear motion part. The overall comparison of the performance of the output torque and force of the 2DoFDDIM at two different linear motion frequencies are presented in Table VI.

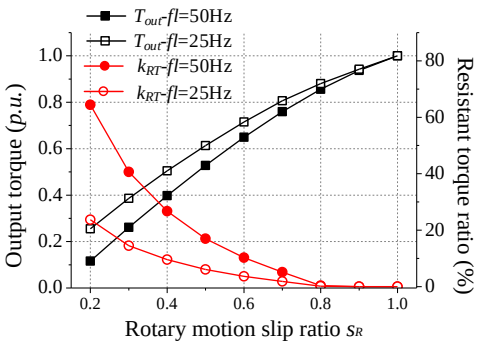

Fig. 14. The output torque and k_{RT} versus different s_r at f_l=25Hz and 50Hz.

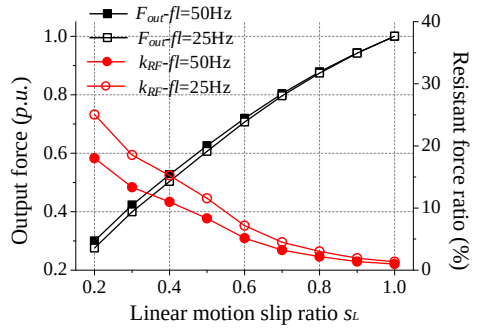

Fig. 15. The output force and k_{RF} versus different s_l at f_l=25Hz and 50Hz.

Therefore, the reduction of the linear motion frequency is an effective strategy, which can be utilized to suppress the helical motion coupling effect in rotary motion part. Meanwhile, the optimized linear motion frequency and axial velocity can be evaluated by the helical motion coupling effect mathematical model. This can be taken into consideration in the preliminary stage of the 2DoFDDIM design to improve the design accuracy.

TABLE VI
PERFORMANCES OF 2DOFDDIM AT TWO LINEAR MOTION FREQUENCIES

Items	Linear motion conditions	
	f_l=50Hz	f_l=25Hz
No-load rotating speed at s_l=0.2 (r/min)	662	702
Locked mover torque at s_l=0.2 (Nm)	11	11
Output torque at s_r=s_l=0.2 (Nm)	1.28	2.6
Resistant torque at s_r=s_l=0.2 (Nm)	2.3	0.8
Resistant torque ratio at s_r=s_l=0.2 (%)	64	23
No-load axial velocity at s_r=0.2 (m/s)	3.81	1.907
Locked mover force at s_r=0.2 (N)	304	181.9
Output force at s_r=s_l=0.2 (N)	91	50.25
Resistant force at s_r=s_l=0.2 (N)	20	16.7
Resistant force ratio at s_r=s_l=0.2 (%)	18	25

C. Experimental verification

To validate the helical motion coupling effect of the 2DoFDDIM, the prototypes of a 12s/2p 2DoFDDIM machine is manufactured as shown in Fig. 16. The main design parameters are in accordance with those listed in Table I. The experiment platform is shown in Fig. 17. A XXX based digital controller is designed to control the prototype machines.

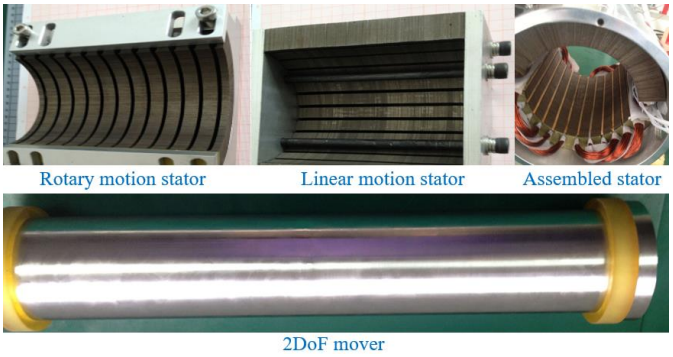

Fig. 16. Prototype of the 2DoFDDIM.

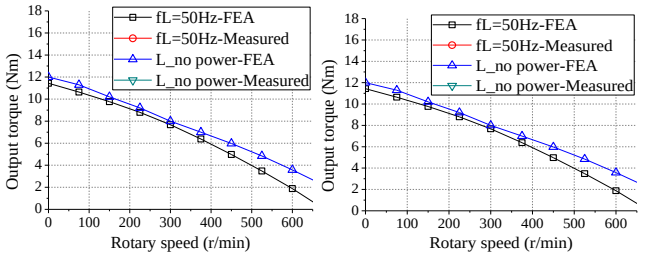

Fig. 17. Measured and predicted torque and force versus different frequency.

The 3D FEA simulated and measured torque-speed curves of 12s/2p 2DoFDDIM is shown in Fig. 17, in which the rated rotating frequency f_r is 50 Hz. It can be found that the measured torque of 2DoFDDIM increases as rotating speed declines, which agrees well with the 3D FEA results. The measured torque of 2DoFDDIM at the rated slip ratio s_r=0.2 is XXNm, which is XX% lower than that of the 3D FEA result. For the helical motion with f_l=50Hz, the measured torque at s_r=0.2 is XXNm, which is XX% of the 3D FEA result. The error between the measured and 3D FEA results in the 2DoFDDIM can be attributed to the prototypes manufacture tolerance and the inaccurate assembling process. In this case, the calculated resistant torque ratio is XX%.

For the helical motion with f_l=25Hz in Fig. 17(b), the measured and 3D FEA torque-speed waveforms are in good agreement. It can be seen that the measured torque at s_r=0.2 is XXNm, which is XX% of that of the 3D FEA result. Then, the resistant torque ratio can be obtained (k_{RT}=XX%). It can be concluded that the helical motion coupling effect in rotary motion part can be suppressed effectively by adjusting the linear motion frequency.

VI. CONCLUSION

This paper investigates the helical motion coupling effect production mechanism in the 2DoFDDIM. The resistant force and torque produced by the coupling effect of rotary and linear motion parts are evaluated. Conclusions are drawn as follow:

(1) The coupling effect torque and force in two motion parts are produced due to the integrated helical motion. The proposed helical motion coupling effect mathematical model can be used to estimate the torque (force) trends effectively.

(2) The coupling effect torque (force) is dominantly determined by the speed of the two motion parts. Besides, it is

worth noting that the flux density of the two motion parts is the key parameter affecting the coupling effect torque (force) at s_r=s_l.

(3) Compared with that of the linear motion part, the torque performance of rotary motion deteriorates more seriously due to the coupling effect. For the rated slip ratio s_r=s_l=0.2, k_{RT} is 64%, which is 3.6 times of k_{RF}.

(4) Based on the coupling effect production mechanism, the coupling effect torque in rotary motion part can be suppressed by two methods, namely adjustment of linear motion slip ratio and change of the linear motion frequency, while the change of the linear motion frequency is more effective and the optimized frequency of linear motion is found to be25Hz.

REFERENCES

[1] T. T. Overboom, J. W. Jansen, E. A. Lomonova, and F. J. F. Tacken, "Design and optimization of a rotary actuator for a two-degree-of-freedom zφ-module," *IEEE Trans. Ind. Appl.*, vol. 46, no. 6, pp. 2401-2409, 2010.

[2] X. Xue, K. W. E. Cheng and Z. Zhang, "Model, analysis, and application of tubular linear switched reluctance actuator for linear comperssors," *IEEE Trans. Ind. Electron.*, vol. 65, no. 12, pp. 9863-9872, 2018.

[3] V.D. Colli, P. Cancelliere, F. Marignetti, R. Di Stefano and M. Scarano, "A tubular-generator drive for wave energy conversion," *IEEE Trans. Ind. Electron.*, vol. 53, no. 4, pp. 1152-1159, 2006.

[4] T. J. Teo, H. Zhu, S.-L. Chen, G. Yang, and C. K. Pang, "Principle and modeling of a novel moving coil linear-rotary electromagnetic actuator," *IEEE Trans. Ind. Electron.*, vol. 63, no. 11, pp. 6930-6940, 2016.

[5] O. Safdarzadeh, A. Mahmoudi, E. Afjei, and H. Torkaman, "Rotary-linear switched reluctance motor: analytical and finite-element modeling," *IEEE Trans. Magn.*, vol. 55, no.5, pp. 8200710, 2019.

[6] S. Li, K. W. E. Cheng, N. Cheung, and Y. Zou, "Design and control of a decoupled rotary-linear switched reluctance motor," *IEEE Trans. Energy Convers.*, vol. 33, no. 3, pp. 1363-1371, 2018..

[7] J. F. Pan, Y. Zou, and N. C. Cheung, "Performance analysis and decoupling control of an integrated rotary-linear machine with coupled magnetic paths," *IEEE Trans. Magn.*, vol. 50, no. 2, pp. 761-764, 2014.

[8] Y. Sato, K. Murakami, and Y. Tsuboi, "Sensorless torque and thrust estimation of a rotational/linear two degrees-of-freedom switched reluctance motor," *IEEE Trans. Magn.*, vol. 52, no. 7, pp. 1-4, 2016.

[9] A. Z. Shukor and Y. Fujimoto, "Direct-drive position control of a spiral motor as a monoarticular actuator," *IEEE Trans. Ind. Electron.*, vol. 61, no. 2, pp. 1063-1071, 2014.

[10] Kaikai Guo and Youguang Guo, "Key parameter design and analysis of flux reversal linear rotary permanent magnet actuator," *IEEE Trans. Appl. Supercond.*, vol. 29, no. 2, pp. 0600405, 2019.

[11] Lei Xu, Chao Zhang and Xiaoyong Zhu, "Decoupling control of a dual-stator linear and rotary permanent magnet generator for offshore joint wind and wave energy conversion system," *IET Electr. Power App.* Vol. 14, no. 4, pp. 561-569, 2020.

[12] Mohammad Mehdi Nezamabadi, Ebrahim Afjei and Hossein Torkaman, "Design, dynamic elecromagnetic analysis, FEM, and fabrication of a new switched-reluctance motor with hybrid motion," *IEEE Trans. Magn.*, vol. 52, no. 4, pp. 8201708, 2016.

[13] Lujia Xie, Jikai Si, Yihua Hu and Zheng Wang, "Overview of 2-degree-of-freedom rotary-linear motors focusing on coupling effect," *IEEE Trans. Magn.*, vol. 55, no.4, pp. 8200611, 2019.

[14] E. Amiri, M. Jagiela, O. Dobzhanski, and E. Mendrela, "Modeling dynamic end effects in rotary armature of rotary-linear induction motor," in *IEEE IEMDC*, USA, pp. 1088-1091, 2013.

[15] Y. Zou, K. E. Cheng, J. Hu, S. Huang, and J. Pan, "A new decoupled rotlin motor with fuzzy sliding mode control," *IEEE Trans. Magn.*, vol. 54, no.11, pp. 8203505, 2018.

[16] Safdarzadeh O., Afjei E. and Torkaman H., "Effective magnetic decoupling control realization for rotary-linear switched reluctance motors utilized in drilling tools," *Int. J. Appl. Electrom.*, vol. 57, no. 3, pp. 257-274, 2018.

[17] L. Xu, M. Lin, X. Fu, X. Zhu, C. Zhang, and W. Wu, "Orthogonal magnetic field analysis of a double stator linear-rotary permanent magnet motor with orthogonally arrayed permanent magnets," *IEEE Trans. Magn.*, vol. 53, no. 11, pp. 1-4, 2017.

[18] Lujia Xie, Jikai Si, Yihua Hu, Haichao Feng and Kai Ni, "Characteristics analysis of the motions of the 2-degree-of-freedom direct drive induction motor," *IEEE Trans. Ind. Electron.*, vol. 67, no. 2, pp. 931-941, 2020.

[19] Gang Lv, Dihui Zeng and Tong Zhou, "An advanced equivalent circuit model for linear induction motors," *IEEE Trans. Ind. Electron.*, vol. 65, no. 9, pp. 7495-7503, 2018.